A Tower-Based Radar Study of Temporal Coherence of a Boreal Forest at P-, L-, and C-Bands and Linear Cross Polarization

Albert R. Monteith, *Member, IEEE*, and Lars M. H. Ulander, *Fellow, IEEE*

***Abstract*— Cross-polarized temporal coherence observations of a boreal forest, acquired using a tower-based radar, are presented in this article. Temporal coherence is analyzed with respect to frequency, temporal baseline, time of day of observation, season, meteorological variables, and biophysical variables. During the summer, P- and L-band temporal coherence exhibited diurnal cycles, which appeared to be due to high rates of transpiration and convective winds during the day. During the winter, freeze-thaw cycles and precipitation resulted in decorrelation. At temporal baselines of seconds to hours, a high temporal coherence was observed even at C-band. The best observation times of the day were midnight and dawn. Temporal coherence is the main limitation of accuracy in interferometric and tomographic forest applications. The observations from this experiment will allow for better spaceborne SAR mission designs for forest applications, better temporal decorrelation modeling, and more accurate forest parameter estimation algorithms using interferometric and tomographic SAR data.**

***Index Terms*— BorealScat, boreal forest, C-band, coherence, decorrelation, L-band, P-band, tower.**

I. Introduction

TEMPORAL coherence is the complex correlation coefficient between two coherent radar observations acquired at different times with the same observation geometry. Temporal coherence is a measure of observation quality for interferometric and tomographic synthetic aperture radar (SAR) applications and a source of information about the observed scene [1]–[5]. A reduction in temporal coherence (temporal decorrelation) is caused by natural and anthropogenic changes in the geometry or dielectric properties of the scatterers within a resolution cell between two observations [6], [7]. Temporal decorrelation in interferometric and tomographic SAR observations is a major limitation to the estimation accuracy of forest parameters, such as tree height and above-ground forest biomass [8]–[11].

The choice of radar parameters affects the temporal coherence. Temporal decorrelation of forest scenes is more severe in high-frequency observations (e.g., C-band: 5400 MHz), which are sensitive to the random movements of unstable scatterers, such as leaves, needles, twigs, and branches. It is generally accepted that temporal coherence decreases as the temporal baseline (time interval between observations) increases because of more meteorological and anthropogenic influences. Therefore, the choice of center frequency and orbital revisit intervals of a spaceborne SAR affects the observed temporal coherence and determines which applications are feasible.

The most common spaceborne implementation of SAR interferometry is by repeated passes over the same scene. Repeat-pass interferometry and tomography will be featured in ESA's upcoming BIOMASS mission for which the primary objective of the mission is to determine the worldwide distribution of forest above-ground biomass [12]. Approximately 36.7% of the boreal forest carbon stock, mainly in Europe and North America, will not be covered due to P-band (435 MHz) transmission regulations [13]. While these regions have well-developed national forest inventory systems, BIOMASS observations are valuable in the remaining Russian boreal forests. BIOMASS will become the spaceborne SAR operating at the lowest center frequency ever [14]. Such a low frequency makes both repeat-pass SAR interferometry (three-day temporal baseline) and tomography (seven passes at three-day intervals) possible. In a tropical forest, it was found that the choice of observation time of day has an impact on the temporal coherence. Temporal coherence was lower during daytime due to higher wind speeds and high evapotranspiration rates [15]. Overpass times of 6 A.M. and 6 P.M. were chosen for BIOMASS to minimize both temporal decorrelation and ionospheric phase scintillations [12], [16].

Currently, the spaceborne SARs with the lowest center frequency (L-band: 1270 MHz) are ALOS-2 (PALSAR-2) and SAOCOM-1A/B. ALOS-2 is in a 12 A.M./12 P.M. polar orbit with a revisit time of 14 days. The L-band successor to ALOS-2, ALOS-4 (PALSAR-3), will have the same orbit. The SAOCOM-1 constellation has a revisit time of eight days. The upcoming L- and S-band SAR, NISAR, will have a dawn-dusk polar orbit with a revisit time of 12 days. The Copernicus High Priority L-band mission, ROSE-L, is planned to consist of two SAR platforms with a global revisit time of six

Manuscript received August 11, 2020; revised January 25, 2021 and March 30, 2021; accepted April 10, 2021. Date of publication May 3, 2021; date of current version December 23, 2021. This work was supported in part by the Hildur and Sven Wingquist Foundation for Forest Research, in part by the European Space Agency (ESA), and in part by the Swedish National Space Agency. *(Corresponding author: Albert R. Monteith.)*

Albert R. Monteith is with the Department of Space, Earth and Environment, Chalmers University of Technology, 41296 Gothenburg, Sweden (e-mail: albert.monteith@chalmers.se).

Lars M. H. Ulander is with the Department of Space, Earth and Environment, Chalmers University of Technology, 41296 Gothenburg, Sweden, and also with the Radar Systems Unit, Swedish Defence Research Agency (FOI), 58111 Linköping, Sweden (e-mail: lars.ulander@chalmers.se).

Digital Object Identifier 10.1109/TGRS.2021.3074098

This work is licensed under a Creative Commons Attribution 4.0 License. For more information, see https://creativecommons.org/licenses/by/4.0/

days [17]. The X-band constellation consisting of TanDEM-X and PAZ allows repeat-pass observations at intervals of at least four days [18]. These long revisit times limit the usefulness of the observations for interferometric forest applications. Most forest applications favor the shortest possible temporal baseline. This comes at the cost of reduced coverage, which is a driver in many other applications. One solution to this problem is to use multiple SAR platforms.

Temporal decorrelation can be eliminated with an instantaneous interferometer, such as TanDEM-X and the proposed L-band mission Tandem-L [19], [20]. Several companion missions extending Sentinel-1 to single-pass interferometry have been proposed [21]–[23]. However, an instantaneous interferometer is not the ideal configuration for all applications. Observations of ocean currents benefit from temporal baselines of milliseconds [24]. Satellite overpasses separated by seconds may also be more favorable than single-pass interferometers for reducing the risk of collisions. Multiple SAR platforms in the same orbit with orbital phase shifts have been implemented, such as the ERS 1/2 tandem phase (one-day temporal baseline), Sentinel-1A/B (six-day temporal baseline), and COSMO-SkyMed ($<$12-h temporal baseline). The long integration times of geosynchronous and geostationary SARs, such as the C-band ESA Earth Explorer 10 candidate, Hydroterra, require high coherence over temporal baselines of minutes to hours [25], [26]. All these SAR missions encompass a wide range of possible temporal baselines.

Temporal decorrelation in forest observations has been attributed to the influence of wind, freeze-thaw cycles, rain, snow, soil moisture content, tree growth, and vegetation moisture content on the radar echoes [27], [28]. Different environmental variables cause temporal decorrelation over different timescales [11]. Long-frozen periods during the winter have been found to be good conditions for forest parameter estimation in boreal forests using L-band and C-band repeat-pass coherence observations [29], [30]. During unfrozen conditions, temporal decorrelation occurred readily due to soil moisture changes, rain, wind, growth-related changes, and variations in tree water content. In [31], it was observed that acquisitions separated by freezing, thawing, and also acquisitions acquired during temperatures above 0 °C resulted in very low coherences at C-band for temporal baselines of three or more days. Even for temporal baselines of one day, weather effects, such as rain, strong wind, inhomogeneous melting of snow, and freezing in between interferometric ERS-1/2 C-band acquisitions, caused severe decorrelation [32]. In [33], P- and L-band observations from a tower-based radar in a tropical forest were analyzed to characterize the temporal coherence in terms of observation time of day, polarization, and season (wet/dry). The main sources of decorrelation were identified to be changes in tree water content, convective winds, and rainfall. The sensitivity of temporal coherence to tree water content variations was supported by electromagnetic model results [34]. A C-band extension to this experiment showed that the temporal coherence can exhibit diurnal cycles due to convective winds and, to a greater extent, high evapotranspiration rates during the day [35], [36]. Temporal coherence is also dependent on polarization. Polarizations that are more sensitive to scattering off stable structures, such as the ground and trunks (e.g., HH and VV), are expected to undergo less temporal decorrelation than polarizations that are sensitive to smaller structures in the upper canopy (e.g., HV and VH) [28], [37].

Existing models of temporal coherence do not capture the dependence on meteorological variables, moisture changes, time of day, or seasons [6], [11], [25]. Dielectric fluctuations have been incorporated in a coherence model at L-band [38], though based on assumptions that lack *in situ* observational support. The dependence of temporal coherence on the temporal baseline in coherence models is also assumed to be monotonically decreasing, which is not always the case [35], [39]. Regarding boreal forests, the lack of a comprehensive understanding of temporal coherence limits the effectiveness of spaceborne SAR mission designs and the performance of forest parameter estimation algorithms. Temporal coherence is difficult to characterize using airborne and spaceborne SAR data due to temporal sparsity and the influence of geometric and volume decorrelation [28]. Temporally dense, multiannual, zero-spatial baseline observations are necessary for gaining a better understanding of temporal decorrelation in boreal forests.

In this study, tower-based radar observations of a boreal forest stand were analyzed to characterize the temporal coherence in terms of the following:

1) frequency (P-, L-, and C-bands);
2) temporal baseline (seconds to weeks);
3) observation time (dawn, dusk, noon, and midnight);
4) season (summer and winter);
5) meteorological and biophysical variables.

Only cross-polarized observations were considered in this study. Cross-polarized observations are expected to have the lowest coherence of all linear polarization combinations. This is because cross-polarized observations originate mainly from depolarizing scatterers that include less stable structures, such as branches. Cross-polarized observations have also been shown to have the closest correlation with forest properties [40] and are always available in the dual-pol mode used to acquire most spaceborne SAR images. Observations were made from a static tower platform (zero-spatial baseline), and thus, measurements were not influenced by geometric or volume decorrelation. Decorrelation introduces multiplicative noise in SAR measurements, which decreases the accuracy of forest parameters estimated from interferometric or tomographic SAR data. The sensitivity of an estimated parameter to this noise depends on the application and algorithm used. Nevertheless, a temporal coherence below 0.8 is typically a significant source of estimation error [33] and is here adopted as a threshold for distinguishing between high and low coherence.

This work is part of the BorealScat radar tower experiment [41]. The main goal of the experiment is to study how radar observations of a boreal forest vary with time. Previous studies have focused on temporal variations in forest backscatter [39], [42]. In the present study, the phase information measured using this coherent radar is included by focusing on the temporal coherence of BorealScat radar observations.

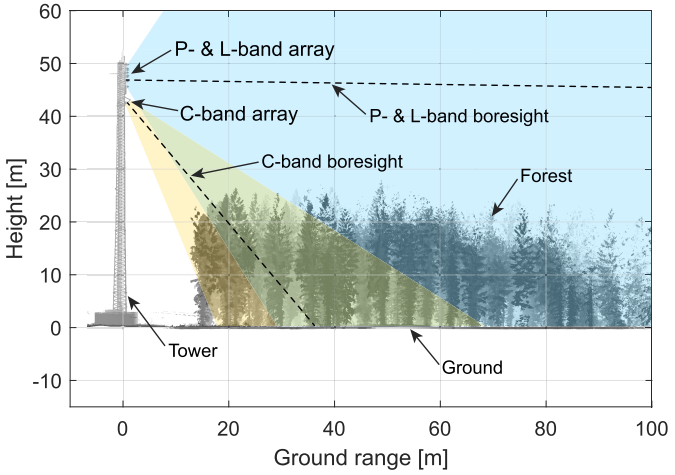

Fig. 1. Illustration (to scale) of the observation geometry in the image plane. The blue region is illuminated by the P- to L-band antennas with a gain of at least −3 dB relative to the maximum antenna gains (6 dBi). The yellow region is illuminated by the C-band antennas with a gain of at least −3 dB relative to the maximum antenna gains (18 dBi).

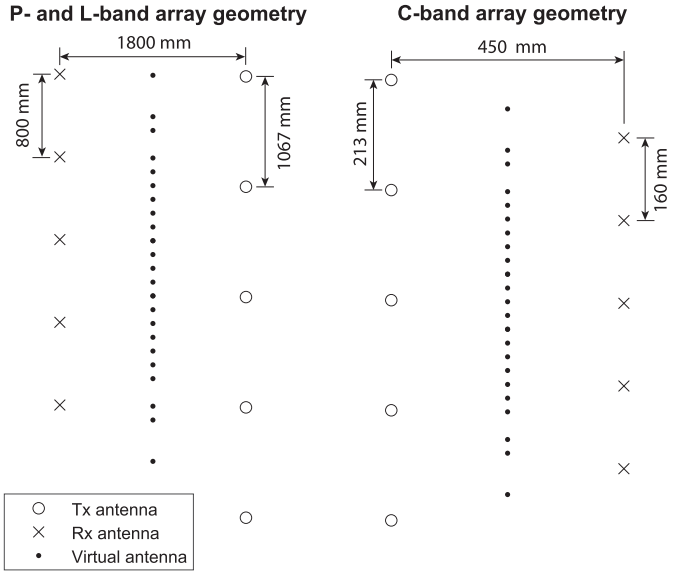

Fig. 2. Geometric configuration (to scale) of antennas in the two arrays for cross-polarized measurements. Positions of virtual monostatic antennas corresponding to the bistatic measurements are also shown. The arrays are viewed from the front in the opposite direction of boresight. The P-/L-band array is vertically mounted, but the C-band array is tilted 50° (depression angle) from the vertical.

First, the experiment setup, observation scheme, and coherence estimation methods are described in Section II. In Section III, temporal coherence results are presented in the order of decreasing temporal baseline. We report the results in terms of median performance, with selected cases presented at the end.

II. Method

A. Radar Measurements

The observed scene is a dense, homogeneous forest stand consisting of mature Norway spruce (*Picea abies* (L.) Karst) with tree heights of 25–27 m. The mossy forest floor is flat and has little understory. The site is located in the Remningstorp experimental forest in southern Sweden. The radar instrument consists of a 20-port vector network analyzer (VNA) connected to an array of 30 antennas mounted at the top of a 50-m high tower overlooking the forest. Fig. 1 shows the observation geometry in the vertical imaging plane. Note that C-band observations are focused on a smaller region close to the tower, whereas P- and L-band observations are acquired over a larger region. The system is designed for tomographic imaging at P-, L-, and C-bands at all linear polarization combinations.

For acquiring a single tomogram, several transmit–receive measurements are taken between antennas in the array. Two columns (one for transmitting and the other for receiving) of five antennas each contribute to a single tomographic image. The same linearly polarized antennas are used for P- and L-bands. For the P- to L-band array measurements, there are four columns in total (20 antennas), giving both a vertically and horizontally polarized column for transmission and reception. For C-band, dual-polarized antennas were used, needing only two columns of antennas (ten antennas) for fully polarimetric measurements. Thus, there are 30 antennas in total. The array geometry for cross-polarized measurements is shown in Fig. 2. For analysis purposes, the transmit–receive combinations may be approximated as virtual antenna positions located halfway between each transmitting and receiving antenna element. The array configuration results in a vertical array of such equivalent virtual monostatic antenna elements. This vertical aperture provides resolution in elevation, whereas the signal bandwidth provides resolution in range. Signal parameters and antenna specifications are listed in Table I for each frequency band. The array does not have a horizontal aperture. Resolution in the cross-range, or azimuth, direction is limited by the antenna beamwidth in the azimuth direction. At P- and L-bands, this beamwidth is at least 60°. As a result, reflections over a height interval (determined by the elevation resolution) from many trees are integrated into the azimuth direction. This is not a problem because the ground is flat and the forest can be considered homogeneous since many trees contribute to the backscatter within the azimuth beamwidth. At C-band, a higher antenna gain was desired to compensate for higher cable losses at C-band. This larger gain came at the cost of narrower beamwidths in elevation and, especially, azimuth, as detailed in Table I. Further details of the instrument design can be found in [41].

TABLE I
SIGNAL PARAMETERS AND ANTENNA SPECIFICATIONS FOR EACH FREQUENCY BAND

Band	Centre frequency [MHz]	Bandwidth [MHz]	Max. antenna gain [dBi]	Half power beamwidth
P	435	30	6	68° (E-plane) 114° (H-plane)
L	1308	135		60° (E-plane) 98° (H-plane)
C	5303	107	18	10° (azimuth) 35° (elevation)

B. Measurement Duration

For a VNA radar, the measurement time is proportional to the signal bandwidth, assuming a fixed unambiguous range.

The measurement time for acquiring a tomogram is 40, 180, and 140 ms for P-, L-, and C-bands, respectively. Temporal decorrelation during these measurement times can be assumed negligible for P- and L-bands for the range of wind speeds observed in this experiment. This is not the case at C-band, where small random movements of a wind-blown canopy can result in large Doppler shifts. Continuous-wave Doppler measurements from the radar tower, similar to those in [43], showed that the C-band coherence decreases to 0.8 within the tomographic measurement time of 140 ms for a mean wind speed between 10 and 11 m/s. For wind speeds above 11 m/s, the correlation time (here defined as the temporal baseline giving a coherence of 0.8) is less than the C-band tomographic image acquisition time, making tomographic images significantly affected by temporal decorrelation. The minimum correlation time that can be measured at C-band using tomographic imaging is, thus, 140 ms. This occurs at relatively high wind speeds for this region, which would result in low coherences even for a perfect instrument. To summarize, each tomogram provides a reliable snapshot of the forest scene, except for C-band acquisitions acquired during high wind speeds.

C. Tomographic Image Formation

This section summarizes the tomographic image formation procedure, including calibration, which is described in detail in [44]. For a transmit–receive antenna pair, the VNA measures a frequency-domain signal $S^{\text{Meas}}(f)$. The frequency f extends over the signal bandwidth in steps of 0.5 MHz. VNA radar measurements are susceptible to a strong mutual antenna coupling component, which must be suppressed for narrow bandwidth measurements (such as the 30-MHz bandwidth P-band measurements) to avoid interference between reflections from the forest scene and sidelobes originating from the strong mutual coupling response near the antennas. The root MUltiple Signal Classification (MUSIC) algorithm was used to separate the strong, impulse-like spectral component of the mutual antenna coupling from the noise-like forest reflections [44]. The root MUSIC algorithm finds the frequencies (ranges in this application) of strong sinusoidal components in $S^{\text{Meas}}(f)$ that have been separated from the background noise and clutter. These sinusoidal components form the estimated mutual coupling component $\hat{\xi}^{\text{Coupling}}(f)$, which was subtracted from the measured signal in the frequency domain according to

$$S^{\text{Cal}}(f) = S^{\text{Meas}}(f) - \hat{\xi}^{\text{Coupling}}(f). \tag{1}$$

The mutual coupling contribution is suppressed in the calibrated frequency-domain signal $S^{\text{Cal}}(f)$. After applying a Hamming window $W_R(f)$ to suppress sidelobes in range, the inverse discrete Fourier transform (iDFT) was used to obtain a range profile

$$x(R) = \text{iDFT}\{W_R(f)S^{\text{Cal}}(f)\} \tag{2}$$

where R is the one-way range from the midpoint between the transmitting and receiving antennas. Having suppressed the mutual coupling component in the frequency domain, sidelobes from the strong impulse-like mutual coupling component do not appear in the range profile $x(R)$. This procedure is repeated for all 25 combinations of five transmitting and five receiving antennas contributing to a tomographic image, which is computed as

$$I(\mathbf{p}) = \frac{1}{H(\mathbf{p})} \sum_{m=1}^{5} \sum_{n=1}^{5} \frac{W_{\text{Array}}^{mn} x^{mn}\left(R_{\mathbf{p}}^{mn}/2\right)}{\hat{C}^{mn}} e^{j2\pi f_c R_{\mathbf{p}}^{mn}/c_0} \tag{3}$$

where $\mathbf{p}$ is a pixel location on the image plane, m is the index of the receiving antenna, n is the index of the transmitting antenna, W_{Array}^{mn} is a window function for suppressing sidelobes in elevation, $R_{\mathbf{p}}^{mn}$ is the two-way antenna-pixel-antenna distance, $j = \sqrt{-1}$, f_c is the center frequency, and c_0 is the speed of light in a vacuum. $\hat{C}^{mn}$ is a factor compensating for magnitude and phase imbalances between antenna pairs and is estimated using the range profile response of a trihedral corner reflector. For P- and L-band, a large corner reflector with short sides of 5 m was placed in an open field beyond the forest. For C-band, a smaller reflector was placed near the base of the tower. The factor $H(\mathbf{p})$ normalizes pixel values for differences in their impulse responses and antenna gains across the image plane [44].

D. Regions of Interest in Tomograms

To increase the number of independent samples, regions of interest were selected from the complex-valued tomographic images for coherence estimation. The regions were selected to be representative of the typical incidence angles of spaceborne SARs (20°–55°). Examples of single-look tomographic images with their regions of interest are shown in Fig. 3. The P-band reflection originates mainly from the upper canopy, with some ground-level scattering. The L- and C-band reflections are dominated by upper canopy scattering. This is because the forest is dense, with very few gaps allowing line-of-sight observation of the ground. The ground is visible at P-band because electromagnetic waves penetrate the canopy more easily compared at L- and C-bands.

As detailed in Section II-A, different signal parameters and array geometries are used for the frequency bands, resulting in large differences in the image resolutions. The slant-range resolution is determined by the signal bandwidth (specified in Table I). The elevation resolution is determined by both the vertical aperture of the array in relation to the wavelength and the angle off the array boresight. The image resolution varies across the image, as shown in Fig. 4. Even though the same antenna array is used for P- and L-band measurements, the L-band images have a finer resolution because of: 1) a wider signal bandwidth and 2) a larger vertical array aperture relative to the signal wavelength. Being aperture limited (unlike beamwidth limited as is the case in SAR), the elevation (or cross-range) resolution degrades as the angle off boresight increases, producing the streaks near the ground in the L-band tomogram. The C-band tomograms have a fine resolution because the array was optimized (in terms of array aperture and tilt angle) for high-resolution forest canopy observations at C-band only. The C-band region of interest does not include the ground since the ground contribution is so weak (due to canopy attenuation) that it is dominated by

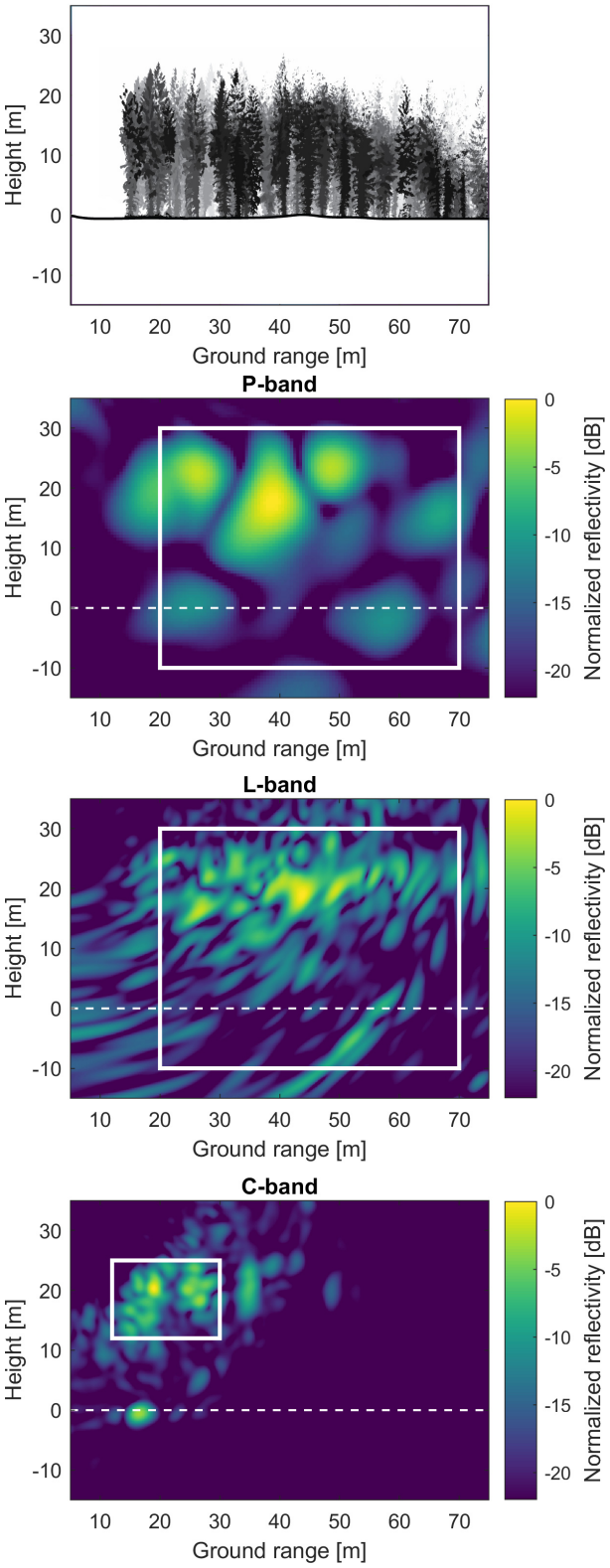

Fig. 3. Top image is a section of a terrestrial LiDAR point cloud near the imaging plane. The lower three images are cross-polarized tomographic images acquired at midnight on June 1, 2018. The white rectangles indicate the regions of interest used for coherence estimation. The dashed line indicates the ground level. The pixel intensities in each tomographic image have been normalized relative to the maximum pixel intensity in the image, making them in units of *normalized reflectivity*.

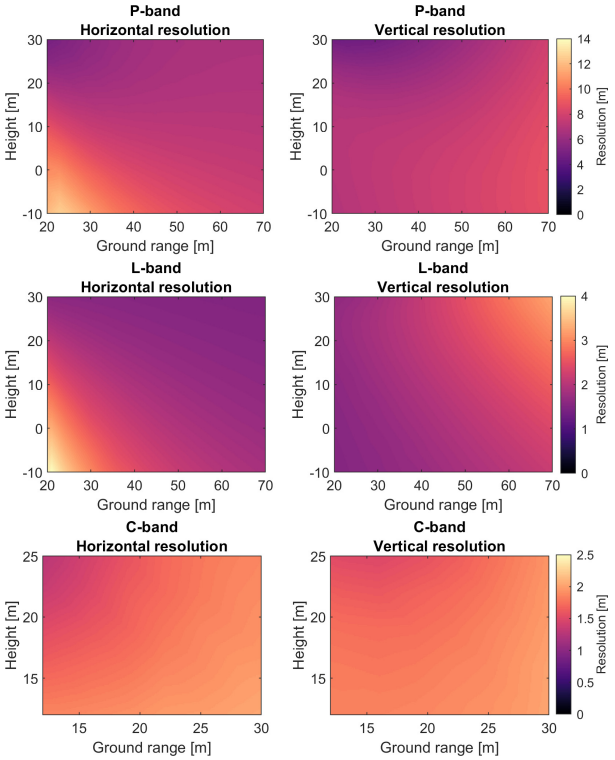

Fig. 4. Tomographic image resolutions within the regions of interest shown in Fig. 3. Resolution is defined as the distance between −3-dB power points (relative to the maximum) of an impulse response in the horizontal and vertical directions. The same color scale is used across each row.

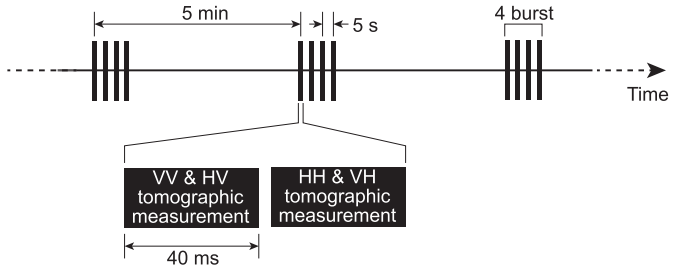

Fig. 5. Timeline of the measurement sequence. Every 5 min, a burst of four tomographic observations were made. Four tomograms for each polarization were thus acquired every 5 min. This figure is reproduced from [42] under the Creative Commons BY 4.0 license (https://creativecommons.org/licenses/by/4.0/).

imaging sidelobes and noise. There is also a trihedral corner reflector on the ground in the C-band images.

E. Temporal Baselines

The measurement sequence consists of a burst of four tomographic measurements repeated every 5 min. This measurement sequence is shown in Fig. 5. The four tomographic measurements in a burst are separated by 5 s. This allows the investigation of temporal changes in radar observations at intervals of 5, 10, and 15 s and multiples of 5 min. These were the temporal baselines investigated in this study. This measurement sequence has been running since September 2017. The main two periods studied are a hot and dry summer

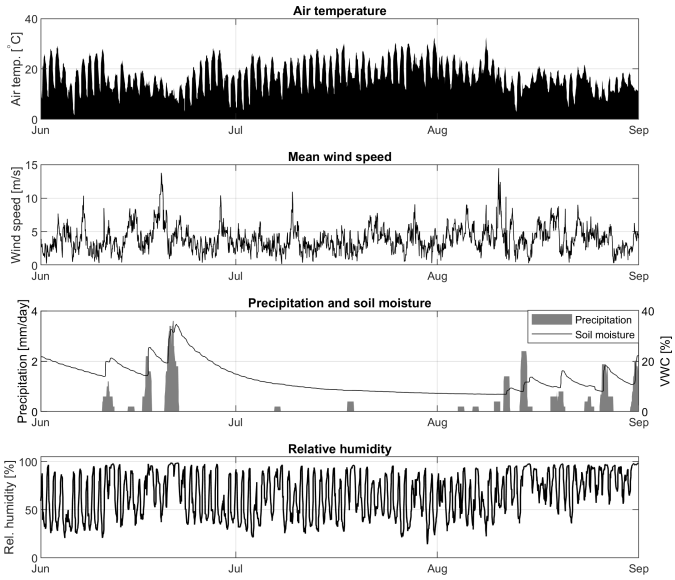

Fig. 6. Meteorological variables and volumetric soil moisture content (VWC) of the summer 2018 period (June 1, 2018–September 1, 2018).

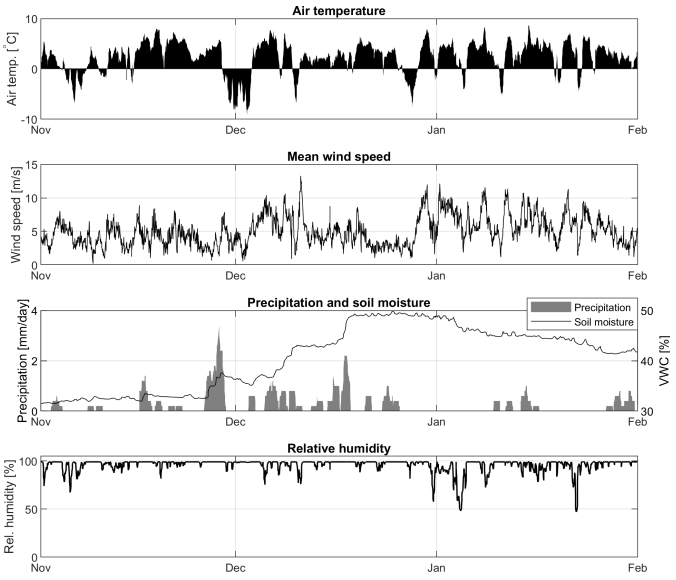

Fig. 7. Meteorological variables and volumetric soil moisture content (VWC) of the winter 2019/2020 period (November 1, 2019–February 1, 2020).

(June 1, 2018 to September 1, 2018) and a wet and windy winter (November 1, 2019–February 1, 2020). Selected examples of temporal coherence from other periods are also presented. All times in this article are local solar times (UTC+54.5 min), which are most relevant for studying the effects of diurnal weather patterns on forest scattering.

F. Ancillary Measurements

An on-site weather station measured air temperature, pressure and humidity, wind speed, and precipitation using a heated rain gauge. This rain gauge cannot distinguish between rain and snow. Wind speed was sampled at intervals of 5 s at a height of 50 m (20 m above the canopy) and averaged over 10 min. Soil moisture was measured in the forest at a single depth within the top 30 cm of the soil. Campbell Scientific CS650 time-domain reflectometry probes were used for measuring soil moisture. While multiple soil moisture probes were installed, data from only one were used in this study. This was due to technical problems. Winters in this region are characterized by frequent freeze-thaw cycles and little snow cover. Meteorological variables and soil moisture content for the main two periods analyzed in this article are shown in Figs. 6 and 7. Measurements of incoming solar radiation, xylem sap flow, and stem radius were included in the final months of the experiment. Sap flow sensors (Implexx Sense) and point dendrometers (Natkon ZN12-T-2WP) were installed at approximately breast height on three trees. The xylem sap flow rate is closely related to the rate of transpiration [45], and variations in the stem radius are related to variations of the stem water content [46].

G. Coherence Estimation

The complex coherence between two bursts, separated by a temporal baseline of a multiple of 5 min, was estimated according to

$$\rho = \frac{\sum_{k=1}^{4}\sum_{p=1}^{P} I_{t1}^{k}(p) I_{t2}^{k}(p)^{*}}{\sqrt{\sum_{k=1}^{4}\sum_{p=1}^{P}\left|I_{t1}^{k}(p)\right|^{2}\sum_{k=1}^{4}\sum_{p=1}^{P}\left|I_{t2}^{k}(p)\right|^{2}}} \tag{4}$$

where k is the index of the measurement in a burst, p is the tomographic image pixel index in the region of interest, P is the number of pixels in a region of interest, $I(p)$ is a tomographic image, $t1$ is the time of the first observation (reference/master), and $t2$ is the time of the second observation (slave). The temporal baseline is equal to $t2 - t1$. The summation over k in (4) implies that all four measurements in a burst are used when estimating the coherence when the temporal baseline is a multiple of 5 min. This is done to maximize the number of samples in the estimate. When estimating the coherence for temporal baselines of 5, 10, and 15 s (between measurements in a burst), the summation over k is not included.

Interpretation of the results presented in this article requires consideration of the coherence estimation accuracy. Coherence estimates computed using (4) have an associated estimation bias and variance that are dependent on the true value of the coherence and the number of independent samples (looks) [47]. The estimated coherence is also reduced by thermal noise by an amount that is dependent on the signal-to-noise ratio (SNR) [1].

Each tomographic image provides a certain number of looks, which is dependent on the antenna array geometry, signal bandwidth, and size of the region of interest. The number of looks within the regions of interest was estimated by simulating 500 tomographic images, each with a different realization of a cloud of 5000 uniformly distributed point scatterers. This simulation considered the same signal, antenna array configuration, antenna patterns, and image formation algorithm as in the actual measurement. The stepped-frequency continuous-wave signal of a VNA lends itself well to frequency-domain simulations. For each of the 500 images, the mean backscatter

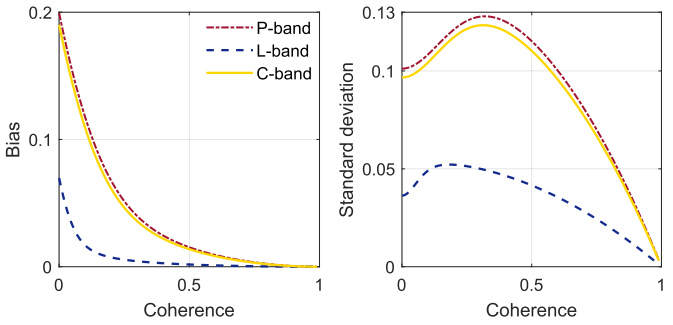

Fig. 8. Bias and standard deviation of the coherence magnitude estimate $|\rho|$ as a function of the true coherence magnitude assuming the estimated number of looks provided by a region of interest (20 for P-band, 162 for L-band, and 22 for C-band). Methods for computing the bias and standard deviation are given in [47]. Note that the curves for P- and C-bands are nearly overlaid.

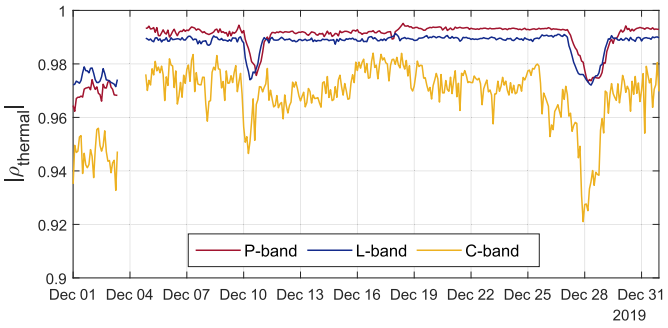

Fig. 9. Thermal coherence for P-, L-, and C-bands during December 2019. The dips in thermal coherence are caused by freezing temperatures which decreases the backscattered power, thereby decreasing the SNR.

over the regions of interest was estimated. The number of looks was estimated as the ratio of the squared mean and the variance of these backscatter estimates [48]. For a single tomographic image, the number of looks provided by the region of interest was estimated to be approximately 20 for P-band, 162 for L-band, and 22 for C-band. The main reason for the L-band number of looks being significantly higher than that of P-band is the finer resolution of L-band images. These are the minimum numbers of looks. The bias and standard deviations of the coherence magnitude estimate $|\rho|$ for the minimum number of looks are shown in Fig. 8. There is a bias of up to 0.2 and a standard deviation of up to 0.13 for low coherences at P- and C-bands. L-band coherence estimates are more accurate. During windy conditions, the trees will move within a burst of four measurements, providing four nearly independent tomographic snapshots of the forest. The number of looks is then up to four times higher for temporal baselines that are multiples of 5 min. This will decrease the bias and standard deviation shown in Fig. 8. Under static (no wind) conditions, all four tomograms in a burst would be equal and the values in Fig. 8 will apply.

The estimated coherence ρ can be decomposed into a temporal coherence factor ρ_{temporal} and a thermal noise coherence factor

$$\rho_{\text{thermal}} = \frac{1}{1 + \text{SNR}^{-1}} \tag{5}$$

such that

$$\rho = \rho_{\text{temporal}} \cdot \rho_{\text{thermal}}. \tag{6}$$

The SNR was estimated from the power within the region of interest P_{ROI} and the noise power P_{noise}. P_{noise} was estimated from a region where no forest reflections, ambiguities, or imaging sidelobes appear (beyond a ground range of 150 m and a height of 50 m). Pixel values in this region are dominated by thermal noise. Noise regions from approximately 1500 images were averaged to provide a reliable estimate of P_{noise}. The two image regions used to estimate P_{ROI} and P_{noise} were equal in area, and the same impulse response weighting was applied to both regions. The SNR could then be estimated as

$$\text{SNR} = \frac{P_{\text{ROI}} - P_{\text{noise}}}{P_{\text{noise}}}. \tag{7}$$

The SNR varies with time because the forest backscatter, or equivalently P_{ROI}, changes with time. The SNR is lowest during frozen conditions when the forest backscatter is at a minimum. This effect is shown in Fig. 9 (December 1–4, 11, and 28, 2019), where frozen conditions cause dips in the magnitude of the thermal noise coherence. The thermal noise coherence magnitude $|\rho_{\text{thermal}}|$ does not drop below 0.92 and therefore does not significantly affect the estimated coherence in this experiment. In the rest of this article, the magnitude of the temporal coherence, $|\rho_{\text{temporal}}|$, will simply be referred to as the coherence.

III. Results

The coherence observations are introduced in Section III-A as temporal coherence matrices, which provide an overall view of the data sets. Thereafter, in Sections III-B–III-E, the median coherence is characterized in the order of decreasing temporal baseline. Finally, in Section III-F, selected cases of coherence time series are discussed.

A. Temporal Coherence Matrices

Temporal coherence matrices provide a representation of how the temporal coherence varies for different temporal baselines ($t2-t1$) and different reference times ($t1$). Temporal coherence matrices for the two observation periods and all three frequency bands are shown in Fig. 10. Values along the diagonal have zero temporal baseline, giving a coherence of 1. Note that this diagonal might not be visible due to the fine sampling interval (1 h) in these plots. The temporal baseline increases as one moves toward the right from the diagonal. Different points along the diagonal represent different reference times, as given by the axis labels. Temporal coherence matrices are symmetric, so to avoid redundancy, only the top half of the matrices are shown.

In general, the P-band coherence was the highest, followed by L-band coherence. During the summer, P-band coherence remained high over the entire observation period, with only a few short events decreasing the coherence. During the winter, the P-band coherence also remained high for several months but decreases significantly when the air temperature drops below 0 °C (e.g., beginning of December 2019), causing moisture in the forest structures to freeze. L-band coherence

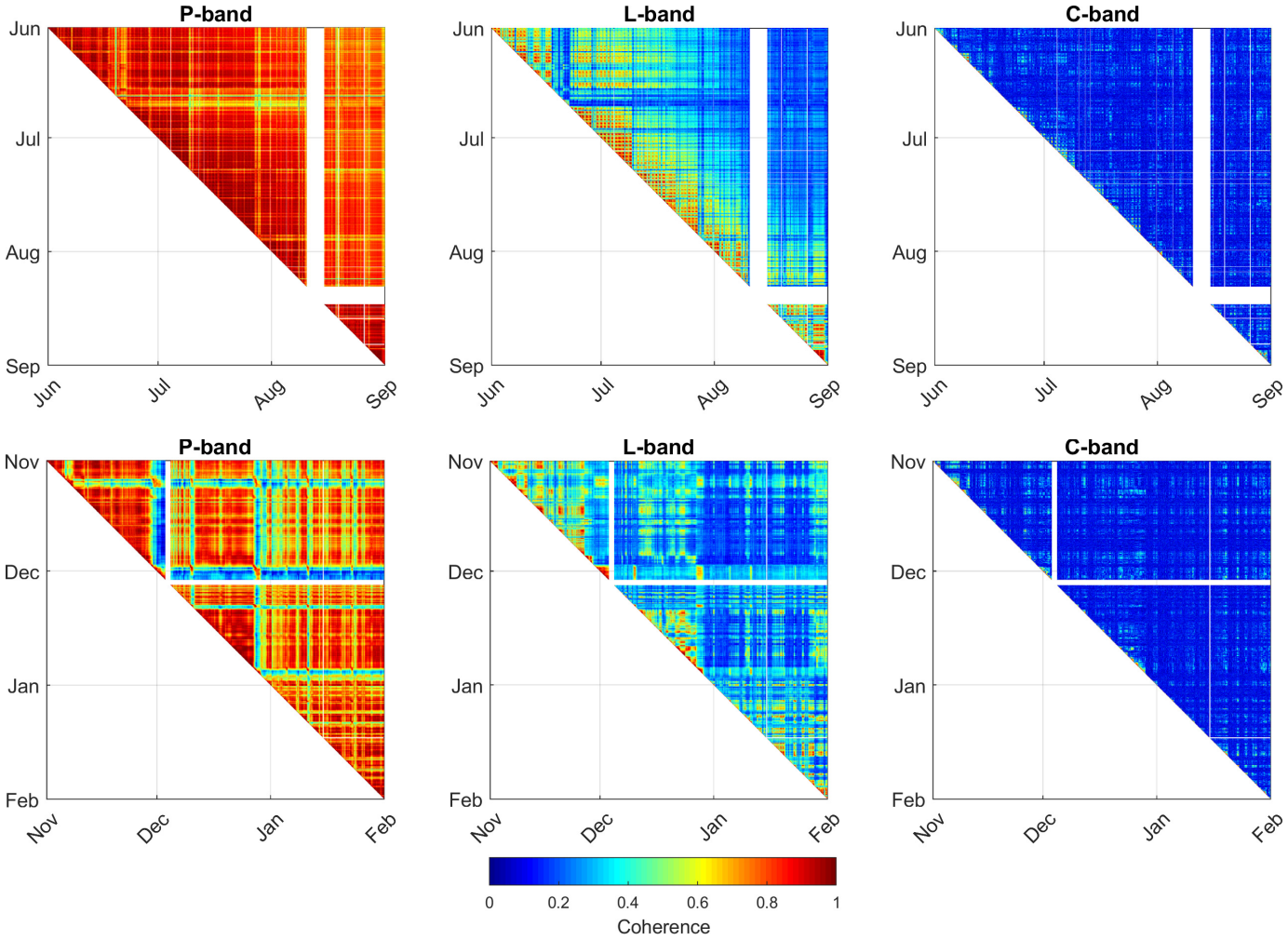

Fig. 10. (Top row) Temporal coherence matrices for the summer 2018 period and (bottom row) the winter 2019/2020 period. The sampling interval is 1 h in these plots, which cannot be resolved by the pixel size in these images. White gaps are due to missing data.

during the summer appears as a grid in the temporal coherence matrix because of diurnal cycles in coherence. The peak coherence decreased to 0.2 within one to two months. During the winter, L-band coherence was sometimes high along the diagonal. This occurred during frozen conditions that lasted for periods of hours to days. For both P- and L-bands, the coherence returned to high values during negative air temperatures whenever the master tomogram was acquired during frozen conditions. The C-band coherence is generally low for the long temporal baselines in Fig. 10.

The scatterplots in Fig. 11 show the likely causes of drops in P-band coherence. During the summer, there is a clear negative correlation between coherence and wind speed, suggesting that wind-induced tree movement is the main cause of temporal coherence drops in the summer. During the winter, the coherence also drops as the wind speed increases. In addition, the coherence drops significantly when the air temperature drops below 0 °C (the reference measurement was taken during unfrozen conditions).

The diurnal cycles in radar observations during the summer result in different temporal coherences depending on the time of day of observations. Fig. 12 shows the temporal coherence

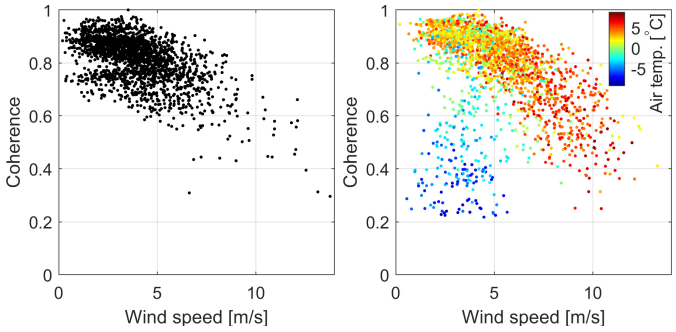

Fig. 11. Scatterplots of P-band temporal coherence during the summer (left) and winter (right). The reference times are 00:00 on June 1, 2018 and November 1, 2019, i.e., the plotted values come from the first rows in the two P-band temporal coherence matrices in Fig. 10. Each point represents one tomogram per hour. P-band coherence decreased due to strong winds in the summer and due to both strong winds and freezing air temperatures during the winter.

matrices for observations during only dawn (6 A.M.), noon (12 A.M.), dusk (6 P.M.), and midnight (12 P.M.) for P- and L-bands during the summer. Each pixel in a row is separated by a temporal baseline of 24 h. The most significant

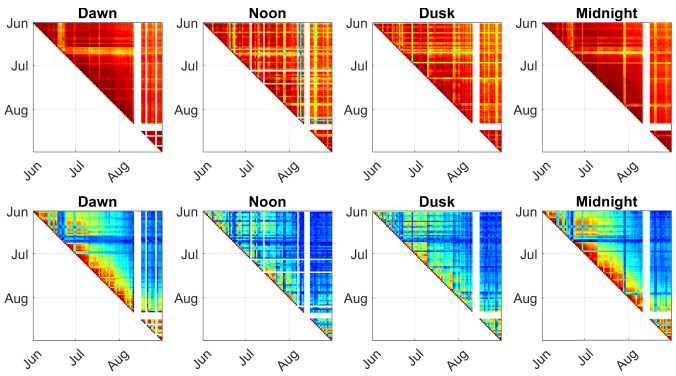

Fig. 12. Temporal coherence matrices for acquisition taken only during dawn (6 A.M.), noon (12 A.M.), dusk (6 P.M.), and midnight (12 P.M.) for the P-band (top row) and L-band (bottom row).

improvement in coherence can be obtained for L-band observations when observing at dawn or midnight when wind speeds and transpiration rates (causing dielectric changes) are at their lowest. For dawn and midnight observations, high L-band coherences were observed for several days. The L-band coherence was much lower for noon and dusk observations. Noon observations yielded the lowest coherences for both P- and L-bands. An improvement in P-band coherence is also observed for dawn and midnight observations compared with other times of the day.

B. Temporal Baselines of Days to Weeks

A statistical representation of how the temporal coherence evolves over temporal baselines of days to weeks can be obtained by selecting samples in a row from the temporal coherence matrices in Fig. 10 that are separated by multiples of one day. Different rows can then be aligned such that the reference times coincide. This gives several coherence estimates for the same temporal baseline. The box plots in Fig. 13 show how the distribution of temporal coherence estimates varies as a function of temporal baseline for 6 A.M. P-, L-, and C-band observations during the summer. When the median approaches 1, the distribution is skewed toward 1. Even though the median is typically high for P-band, some samples can be much lower. As observed for L-band, a median coherence of 0.8 can mean that several observations have a coherence close to 1. As the temporal baseline increases, the median coherence decreases, and the distribution becomes less skewed toward 1. At very low coherences, such as those for C-band in Fig. 13, the distribution is skewed toward 0. This coherence-dependent skewness is a result of the underlying Gaussian-like process from which a finite number of independent samples are used to estimate the coherence [47]. The median never reaches 0 because of the positive bias at low coherences (see Fig. 8). Only the median coherence will be reported from here on. However, it is important to keep the behavior of the distributions in mind.

The median temporal coherence for all three frequency bands and both observation periods is shown in Fig. 14. For a temporal resolution of one day, the coherence dropped monotonically in all cases. P-band coherence was always

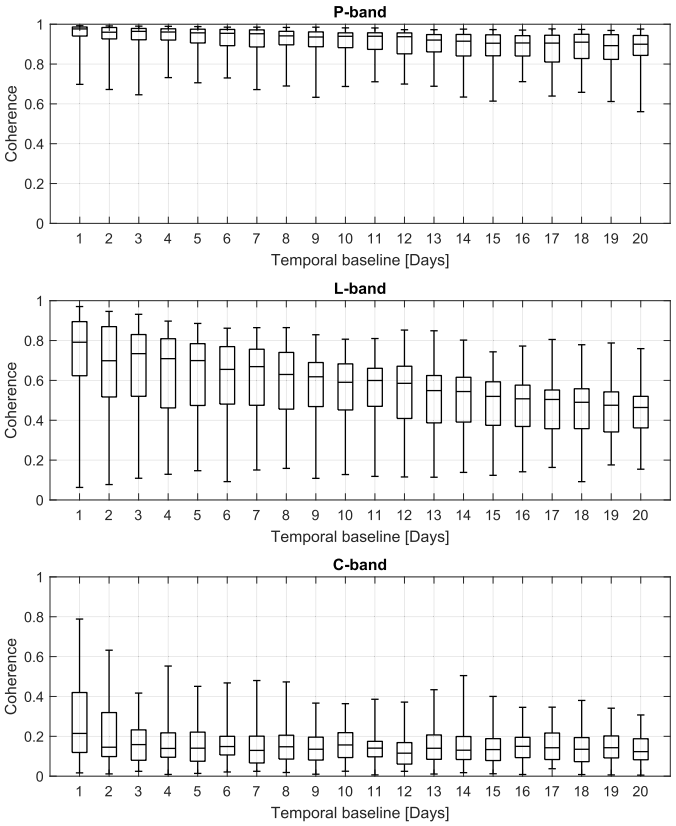

Fig. 13. Box plots of the P-, L-, and C-band temporal coherence over temporal baselines of multiples of one day for 6 A.M. observations during the summer. The box edges indicate the 25th and 75th percentiles. The central mark indicates the median and the whiskers indicate the maximum and minimum.

highest, followed by L-band and then C-band. The temporal coherence was also higher during the summer than during the winter for both P- and L-bands. This may be explained by more frequent precipitation, higher wind speeds, and freeze-thaw cycles during the winter compared with the summer. C-band coherence was low for temporal baselines of one day and more regardless of season. The P-band coherence was high for all reference times, but during the summer, the highest coherences were observed for 6 A.M. and 12 P.M. observations. This is even clearer for L-band summertime coherence, where the median dawn and midnight coherence is near 0.7 for approximately five days. The observation time of day did not significantly affect the coherence during the winter.

C. Temporal Baselines of Hours to Days

The median coherence over timescales of hours to days is shown in Fig. 15. During the winter, the coherence decreases monotonically for all frequency bands as the temporal baseline increases. During the summer, diurnal cycles are seen in all three frequency bands. These cycles are clearest for 6 A.M. and 12 P.M. reference times, after which the coherence decreases during the day and increases again during the night and morning. The recovery in temporal coherence after 24 h is especially strong for L-band. Some coherence recovery is also seen for C-band for 6 A.M. and 12 P.M. reference times, although the median coherence is still low. For 12 P.M.

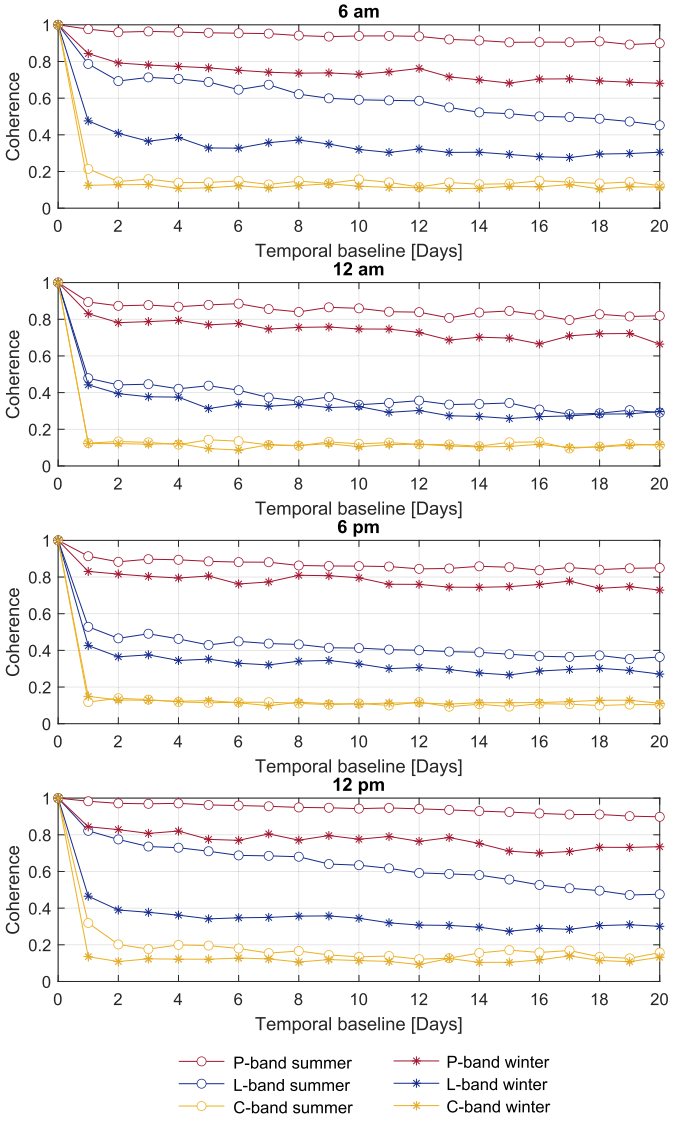

Fig. 14. Median temporal coherence over temporal baselines of multiples of one day. The title of each plot gives the observation time of day.

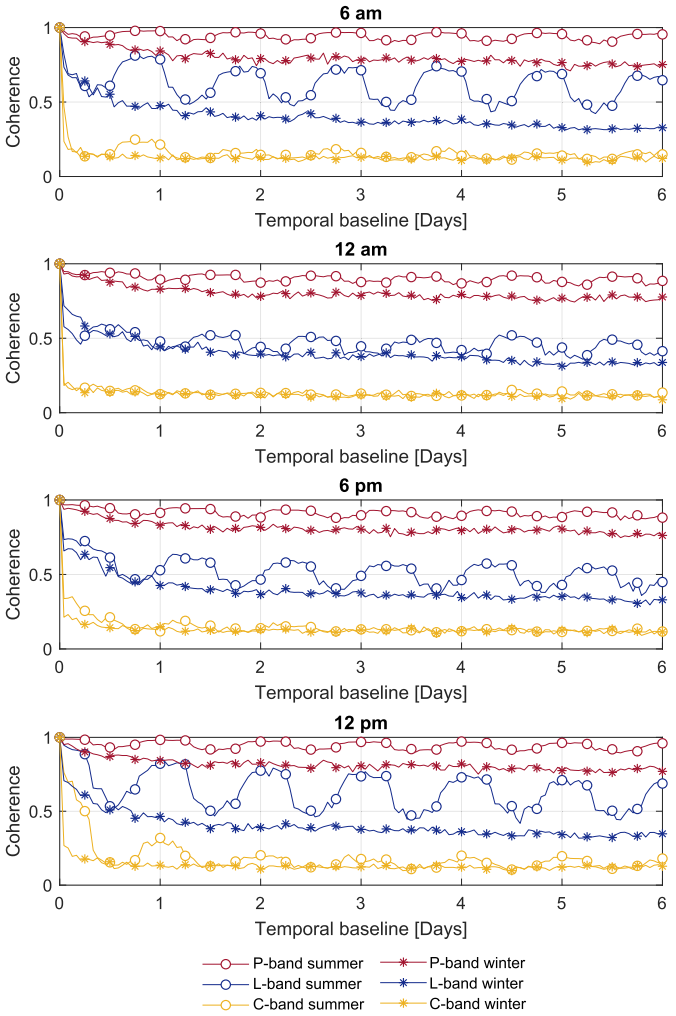

Fig. 15. Median temporal coherence over temporal baselines of hours to days. The title of each plot gives the time of day of the reference observation. Markers are placed at 6-h intervals.

reference times during the summer, the L-band coherence remains high for approximately 6 h (up to 6 A.M.), after which it drops significantly before recovering again after a temporal baseline of 24 h. A similar behavior is observed for C-band, albeit with much lower coherence.

D. Temporal Baselines of Minutes to Hours

Fig. 16 shows a close-up of the coherence over 24 h with a temporal resolution of 5 min. The P-band median coherence was close to 1 throughout the first 24 h, with summer coherences being slightly higher. The median L-band coherence during the summer remained above 0.8 for approximately 1 h after a 6 A.M. acquisition, recovering to and remaining near 0.8 after 15 h (21:00). Even more favorable L-band conditions were seen for 12 P.M. reference times during the summer, where the median coherence remained above 0.8 for 7 h (07:00), recovering again above 0.8 after 20 h (20:00). The median L-band coherence remained between 0.5 and 0.7 for 12 A.M. and 6 P.M. reference times during the summer and for all reference times during the winter. For C-band observations during the summer, 12 P.M. reference times yielded a median coherence above 0.8 for 1 h and above 0.7 for 2 h. For 6 A.M. observations, the C-band median coherence was between 0.5 and 0.7 during the first hour. For other reference times and during the winter, the C-band coherence was poor on timescales of 5 min and longer.

E. Temporal Baselines of Seconds

Temporal coherence for temporal baselines as short as seconds is dominated by wind-induced tree movement. Fig. 17 shows that above a certain threshold, coherence is correlated with wind speed for a temporal baseline of 5 s. The wind speed threshold and amount of decorrelation over such short timescales depends on the frequency. Coherence estimates become more scattered at higher wind speeds. This may be due to a larger estimation variance for lower coherences (see Fig. 8) or the mean wind speed may be less representative of the instantaneous wind speed. The median coherence for P-, L-, and C-bands for temporal baselines of 5–15 s is

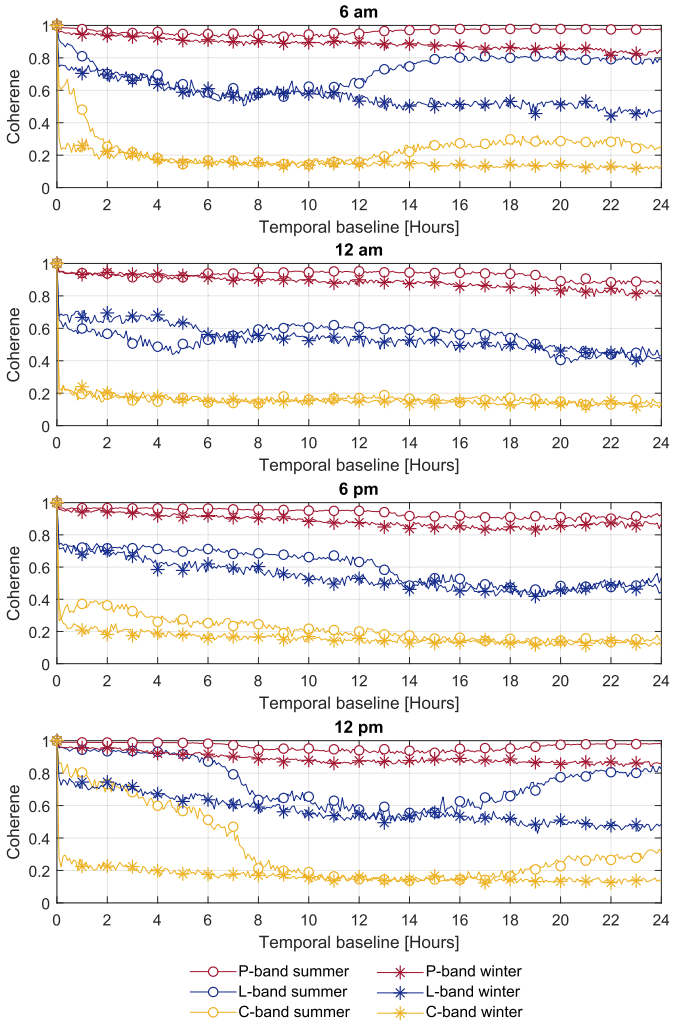

Fig. 16. Median temporal coherence over temporal baselines of minutes to hours. The title of each plot gives the time of day of the reference observation. Markers are placed at 1-h intervals.

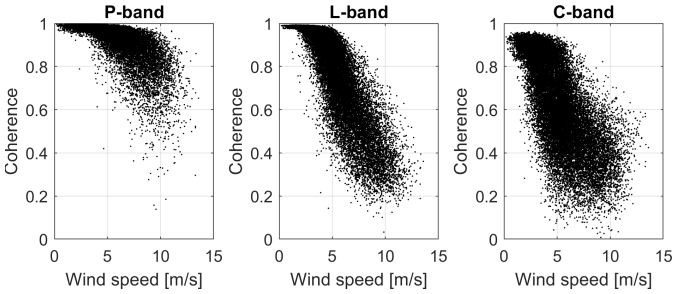

Fig. 17. Temporal coherence versus wind speed for a temporal baseline of 5 s during the winter period. Above a certain threshold, wind speed (measured at a height of 50 m) is correlated with coherence.

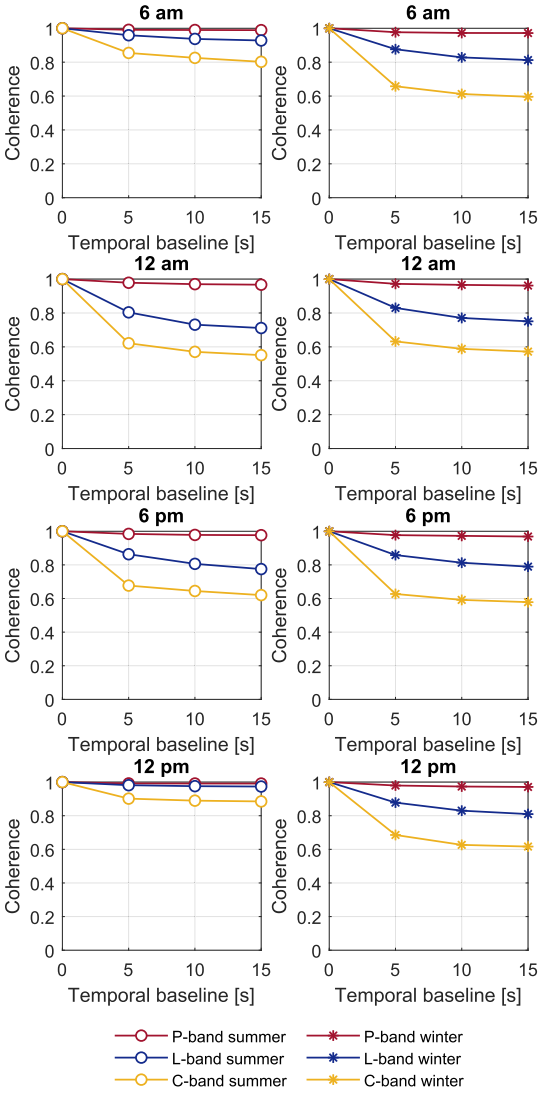

Fig. 18. Median temporal coherence over temporal baselines of multiples of 5 s for the summer (left column) and winter (right column). The title of each plot gives the time of day of the observation.

shown in Fig. 18. The coherence was significantly higher for 6 A.M. and 12 P.M. observations during the summer due to the lower convective wind speeds and transpiration rates during the night and early morning. For other reference times and winter observations, there were little differences in the median coherence. In all cases, the temporal coherence decreased exponentially with increasing temporal baseline, which is characteristic of temporal coherence models assuming stationary stochastic scattering properties. L-band coherence remained near 0.8, but the C-band coherence dropped to below 0.8 for temporal baselines as short as 5 s during the winter and during summer days.

F. Temporal Coherence Time Series

The results presented thus far have provided a statistical sense of how temporal coherence varies as a function of temporal baseline, time of observation, season, and frequency. In this section, examples of temporal coherence time series are shown to gain a better understanding of how temporal coherence is affected by meteorological and biophysical variables. In the following coherence time series plots (see Figs. 19–23), the coherence is computed relative to the starting time (first value on the horizontal axis) of the presented time series. This reference time (master acquisition time) for each plot is specified in the figure caption.

In Fig. 19, large daytime drops in L- and C-band coherence are seen, along with meteorological variables and

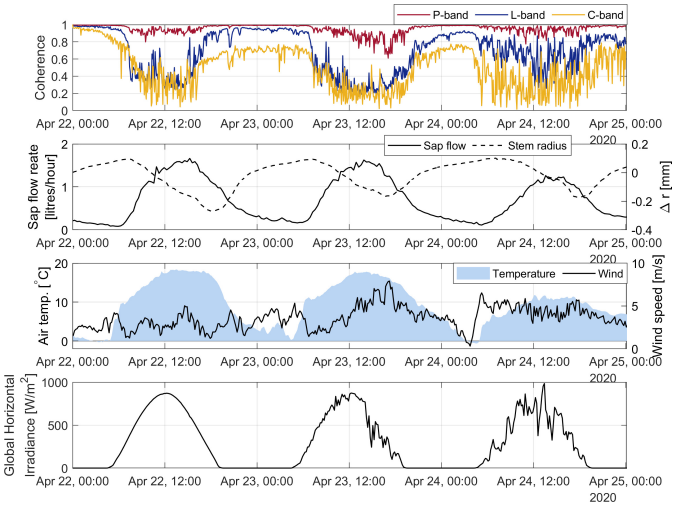

Fig. 19. Time series showing diurnal cycles in temporal coherence during the spring of 2020. The wind speed does not vary diurnally, suggesting that the daytime drop in coherence is caused by tree water transport. The reference time is 00:00 on April 22, 2020.

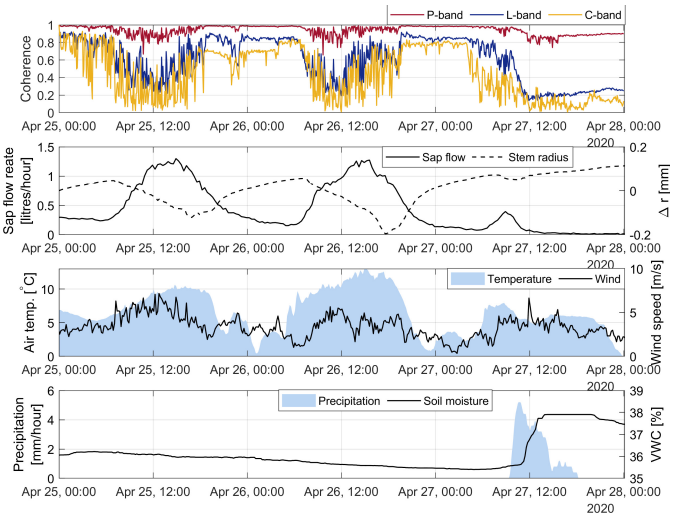

Fig. 20. Time series showing how rainfall causes decorrelation at P-, L-, and C-bands, interrupting diurnal cycles. The reference time is 00:00 on April 25, 2020.

measurements of the tree sap flow and stem radius variations Δr. The wind speed during this period did not vary diurnally and is, therefore, not the cause of the diurnal decorrelation pattern seen in all frequency bands. A low temporal coherence during the day coincided with a high sap flow rate (high rate of transpiration), suggesting that tree water transport within trees was the cause of decorrelation. The stem radius variations were not in phase with temporal coherence cycles, indicating that it was not the change in stem water content that caused decorrelation, but instead the rate of change of water content (sap flow rate). A change in crown water content during transpiration is also a likely cause of decorrelation.

The effect of rainfall is shown in Fig. 20. Rain halts transpiration and breaks the diurnal cycle. It caused large drops in L- and C-band coherence but resulted in little decorrelation at P-band. In the evening of April 28, 2020, the rain stopped, but the P-band coherence did not recover to near 1 again. This can be explained by the observed increase in soil moisture content due to rainfall. L- and C-band coherence also did not recover to high values, despite the low wind speeds toward the end of the time series. This may be due to intercepted rainfall or dielectric changes within the vegetation after rainfall.

Temporal coherence time series from the coldest period of the experiment are shown in Fig. 21. C-band observations are not available from this period. P- and L-band coherence both dropped slowly during frozen conditions. This may be due to increasing ice fractions in the soil and trees as frozen conditions persist with time. P-band coherence recovered to higher values than that of L-band after thawing and refreezing. The wind speed increased above 5 m/s on several occasions in Fig. 21, which tends to cause decorrelation at L-band during nonfrozen conditions (see Fig. 17). This is not the case in Fig. 21, indicating that frozen conditions increase the number of gaps in the canopy of this dense forest, revealing more ground that dominates the coherence.

Another example of coherence during frozen conditions is shown in Fig. 22. P-band coherence appears more sensitive

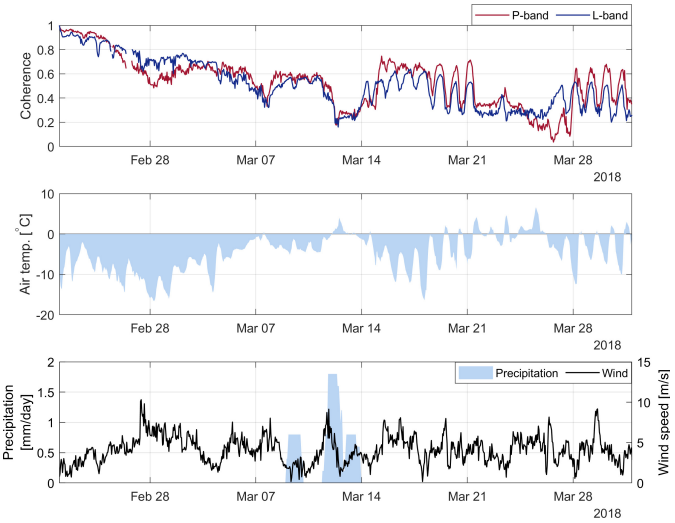

Fig. 21. Time series showing how coherence drops very slowly during long-frozen periods and how the temporal coherence can recover after thawing and refreezing. The reference time is 00:00 on February 22, 2018.

to temperature variations during frozen conditions. This can be explained by greater sensitivity to the varying ice fractions in tree stems and the soil as the temperature changes. The ice fraction in inhomogeneous mixtures such as soil and wood increase with decreasing temperature, resulting in a drop in electric permittivity and change in scattering amplitude [49]–[51]. The L-band coherence did not drop significantly over this period. The largest change in L-band coherence was on February 26, 2020, during which much of the snow on the trees melted. This can be seen in photographs of the forest taken by a camera on the tower. During the three-day period, snow on the ground partially melted. It cannot be concluded that the melting snow had a significant effect on temporal coherence because the dielectric properties of the scene vary as a function of air temperature, especially when near 0 °C. The C-band coherence was very low during this period, most likely because of the moderate wind speed during the reference observation.

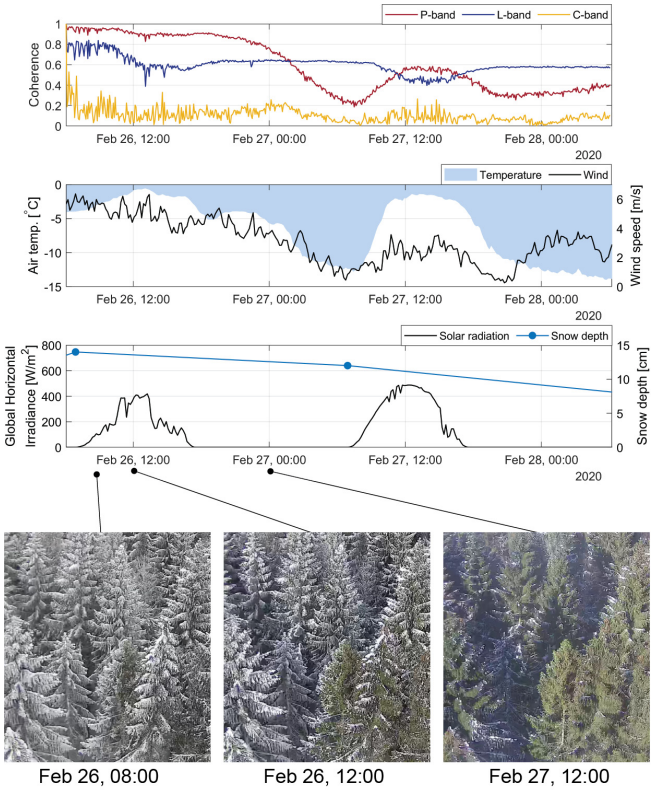

Fig. 22. Time series showing the drop in coherence over a period during which snow melts. P-band coherence appears more sensitive to temperature variations during freezing conditions. The reference time is 04:00 on February 26, 2020. The photographs were acquired by a camera on the tower viewing the forest region observed by the radar.

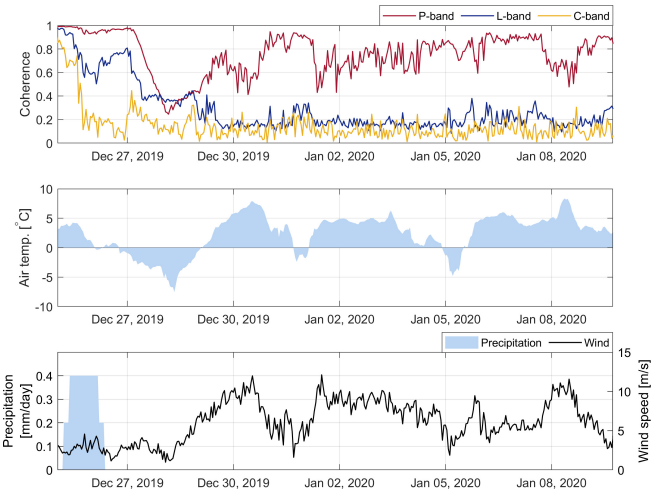

Fig. 23. Time series showing the drop in L- and C-band coherence due to rainfall and a P- and L-band decorrelation due to freezing. During nonfrozen conditions, P-band coherence remains high, but the strong winds cause decorrelation at L- and C-bands. The reference time is 23:55 on December 24, 2019.

The effect of freezing on coherence is shown in Fig. 23. Soon after the reference observation, the L- and C-band observations decorrelated due to rainfall. Surveillance camera images confirmed that the measured precipitation was rain. Thereafter, the temperature dropped below 0 °C (December 27), causing further decorrelation at L-band and significant decorrelation at P-band. After thawing, the P-band coherence returned to high values, but the L- and C-band coherence remained low because of the strong winds. The strong winds also caused some decorrelation at P-band.

IV. Discussion

The results demonstrate that the temporal decorrelation in boreal forests is dependent on several environmental factors. The P-band temporal coherence was observed to be high over temporal baselines of several days and in some cases even several weeks, during both seasons. In a dawn-dusk polar orbit, the likelihood of severe temporal decorrelation in BIOMASS observations is small. During the summer, 6 A.M. observations were observed to be more stable than 6 P.M. observations. During the winter, freezing and temperature variations during freezing conditions caused decorrelation. P-band coherence was not observed to be very sensitive to precipitation, and only strong winds (mean wind speeds greater than about 6 m/s) resulted in significant decorrelation. High transpiration rates and tree water content variations did not appear to cause significant decorrelation at P-band.

L-band temporal coherence was observed to be highly dependent on the time of observations, season, and temporal baseline. The highest temporal coherences for temporal baselines of up to a week were observed during the summer for 6 A.M. and 12 P.M. acquisitions. This was mainly due to wind and a high rate of transpiration during the day. Repeat-pass missions, such as ALOS-2 and ALOS-4 in noon/night polar orbits, therefore, have a high likelihood of acquiring high coherence observations over a temporal baseline of one week when considering ascending (nighttime) passes during the summer. Daytime observations (12 A.M. and 6 P.M.) and observations during the winter yielded, on average, poor L-band coherences for temporal baselines of one day or more. The poor L-band temporal coherence observed during the winter was due to the frequent freeze-thaw cycles and strong winds in this region, instead of long-frozen periods as in previous boreal forest studies. For tandem configurations, temporal baselines up to 3 h with overpasses during the night or early morning are feasible. For temporal baselines of 5–15 s, L-band temporal decorrelation was negligible during the night and early morning during the summer. High transpiration rates during the spring and summer appeared to cause significant decorrelation at L-band. L-band coherence was also sensitive to rainfall. During frozen conditions, L-band coherence was observed to decrease slowly with time and was less sensitive to subzero temperature variations than P-band. L-band coherence was most sensitive to wind, with average wind speeds approaching 10 m/s causing total decorrelation.

Very low temporal coherences were observed at C-band for temporal baselines of one day or more. Repeat-pass interferometric and tomographic applications at C-band are, therefore, not feasible in the environmental conditions that were present in this study. Some increase in coherence was observed after approximately 24 h for night and dawn observations during the summer, but the likelihood of high coherence observations over such temporal baselines was still very low in this forest.

C-band interferometry only becomes feasible over temporal baselines of hours during the summer for night and early morning overpasses. A high likelihood of C-band temporal coherence can only be guaranteed for temporal baselines on the order of seconds. This motivates the implementation of C-band tandem missions flying in close formation. Total decorrelation at C-band was observed after light rainfall and wind speeds approaching 5 m/s.

Only cross-polarized observations were analyzed in this study. Cross-polarized observations have been shown to be very useful for forest parameter estimation but are the most sensitive to temporal decorrelation of all the linear polarization combinations. The results from this study can, therefore, be considered to be of the worst case. Like-polarized data (HH and VV) have also been collected in this experiment. An analysis of the like-polarization data is possible, but considered too extensive to include in the present article and is therefore left for a future publication.

The exact effect of temporal decorrelation on SAR image formation using long integration times, as is necessary in geosynchronous SARs, remains to be investigated. Coherent image formation includes coherent averaging effects, whereby permanent scatterers (also called the dc component) are coherently integrated over time. This effect may offer robustness to temporal decorrelation during long integration times and reduce defocusing of SAR images.

In this experiment, a single forest stand in southern Sweden was observed. To also capture the temporal characteristics of radar observations at higher latitudes, the experiment will be relocated to a forest in northern Sweden. A complementary ground-based SAR has also been established in Northern Finland [52].

V. Conclusion

Temporal decorrelation is a major limitation in forest applications of interferometric and tomographic SAR data. To gain a better understanding of the characteristics of temporal decorrelation in boreal forests, tower-based observations with fine temporal resolution and zero-spatial baseline were analyzed in this study.

Temporal coherence at P-band was observed to be high over temporal baselines of several days, and several weeks for 6 A.M. summer observations, allowing repeat-pass interferometry and tomography. For L- and C-bands, the temporal coherence was much more dependent on the time of day of observation and the season. The best conditions resulting in the highest temporal coherence at L-band were during the night and early morning in the summer. Due to irregular weather conditions at this site, there were no particularly favorable conditions for repeat-pass L-band observations during the winter. In general, the likelihood of high-quality interferometric observations at C-band for temporal baselines exceeding a few seconds is low. This is a strong motivation for the implementation of tandem L- and C-band missions flying in close formation.

The results presented in this article are useful for the design of future spaceborne SAR missions for high-quality interferometric and tomographic observations. The results also present a starting point for better temporal coherence modeling. These efforts will lead to more accurate forest parameter estimates using interferometric and tomographic SAR data.

References

[1] H. A. Zebker and J. Villasenor, "Decorrelation in interferometric radar echoes," *IEEE Trans. Geosci. Remote Sens.*, vol. 30, no. 5, pp. 950–959, Sep. 1992.

[2] E. Rodriguez and J. M. Martin, "Theory and design of interferometric synthetic aperture radars," *IEE Proc. F Radar Signal Process.*, vol. 139, no. 2, pp. 147–159, Apr. 1992.

[3] J. O. Hagberg, L. M. H. Ulander, and J. Askne, "Repeat-pass SAR interferometry over forested terrain," *IEEE Trans. Geosci. Remote Sens.*, vol. 33, no. 2, pp. 331–340, Mar. 1995.

[4] R. Bamler and P. Hartl, "Synthetic aperture radar interferometry," *Inverse Problems*, vol. 14, no. 4, pp. R1–R54, 1998.

[5] R. N. Treuhaft, S. N. Madsen, M. Moghaddam, and J. J. van Zyl, "Vegetation characteristics and underlying topography from interferometric radar," *Radio Sci.*, vol. 31, no. 6, pp. 1449–1485, 1996.

[6] M. Lavalle, M. Simard, and S. Hensley, "A temporal decorrelation model for polarimetric radar interferometers," *IEEE Trans. Geosci. Remote Sens.*, vol. 50, no. 7, pp. 2880–2888, Jul. 2012.

[7] H. Aghababaei *et al.*, "Forest SAR tomography: Principles and applications," *IEEE Geosci. Remote Sens. Mag.*, vol. 8, no. 2, pp. 30–45, Feb. 2020.

[8] S. R. Cloude and K. P. Papathanassiou, "Polarimetric SAR interferometry," *IEEE Trans. Geosci. Remote Sens.*, vol. 36, no. 5, pp. 1551–1565, Sep. 1998.

[9] M. Santoro and O. Cartus, "Research pathways of forest above-ground biomass estimation based on SAR backscatter and interferometric SAR observations," *Remote Sens.*, vol. 10, no. 4, p. 608, 2018.

[10] K. P. Papathanassiou and S. R. Cloude, "The effect of temporal decorrelation on the inversion of forest parameters from Pol-InSAR data," in *Proc. IEEE Int. Geosci. Remote Sens. Symp. (IGARSS)*, Toulouse, France, vol. 3, Jul. 2003, pp. 1429–1431.

[11] J. I. H. Askne, P. B. G. Dammert, L. M. H. Ulander, and G. Smith, "C-band repeat-pass interferometric SAR observations of the forest," *IEEE Trans. Geosci. Remote Sens.*, vol. 35, no. 1, pp. 25–35, Jan. 1997.

[12] S. Quegan *et al.*, "The European space agency BIOMASS mission: Measuring forest above-ground biomass from space," *Remote Sens. Environ.*, vol. 227, pp. 44–60, Jun. 2019.

[13] J. M. B. Carreiras *et al.*, "Coverage of high biomass forests by the ESA BIOMASS mission under defense restrictions," *Remote Sens. Environ.*, vol. 196, pp. 154–162, Jul. 2017.

[14] *Report for Mission Selection: BIOMASS. ESA SP-1324/1 (3 volume series)*, Eur. Space Agency, Noordwijk, The Netherlands, 2012.

[15] D. H. T. Minh *et al.*, "Tropiscat: Multi-temporal multi-polarimetric tomographic imaging of tropical forest," in *Proc. Int. Geosci. Remote Sens. Symp. (IGARSS)*, Munich, Germany, Jul. 2012, pp. 7051–7054.

[16] P. Snoeij, N. Van Der Valk, E. Boom, and D. Hoekman, "Effect of the ionosphere on P-band spaceborne SAR images," in *Proc. Int. Geosci. Remote Sens. Symp. (IGARSS)*, Sydney, NSW, Australia, vol. 1, Jul. 2001, pp. 132–134.

[17] M. Davidson *et al.*, *Copernicus L-Band SAR Mission Requirements*, document ESA-EOPSM-CLIS-MRD-3371, Earth Mission Science Division, European Space Agency, 2018.

[18] F. Sica *et al.*, "InSAR decorrelation at X-band from the joint TanDEM-X/PAZ constellation," *IEEE Geosci. Remote Sens. Lett.*, early access, Aug. 19, 2020, doi: 10.1109/LGRS.2020.3014809.

[19] G. Krieger *et al.*, "TanDEM-X: A satellite formation for high-resolution SAR interferometry," *IEEE Trans. Geosci. Remote Sens.*, vol. 45, no. 11, pp. 3317–3341, Nov. 2007.

[20] A. Moreira *et al.*, "Tandem-L: A highly innovative bistatic SAR mission for global observation of dynamic processes on the earth's surface," *IEEE Geosci. Remote Sens. Mag.*, vol. 3, no. 2, pp. 8–23, Jun. 2015.

[21] A. Regan, P. Silvestrin, and D. Fernandez, "Sentinel convoy: Synergetic earth observation with satellites flying in formation with European operational missions," in *Proc. Living Planet Symp.*, vol. 740, Aug. 2016, p. 379.

[22] H. Rott *et al.*, "SESAME: A single-pass interferometric SEntinel-1 companion SAR mission for monitoring GEO-and biosphere dynamics," in *Proc. IEEE Int. Geosci. Remote Sens. Symp. (IGARSS)*, Fort Worth, TX, USA, Jul. 2017, pp. 107–110.

[23] P. López-Dekker, H. Rott, P. Prats-Iraola, B. Chapron, K. Scipal, and E. De Witte, "Harmony: An Earth explorer 10 mission candidate to observe land, ice, and ocean surface dynamics," in *Proc. IEEE Int. Geosci. Remote Sens. Symp. (IGARSS)*, Yokohama, Japan, Aug. 2019, pp. 8381–8384.
[24] A. Elyouncha, L. E. B. Eriksson, R. Romeiser, and L. M. H. Ulander, "Measurements of sea surface currents in the baltic sea region using spaceborne along-track InSAR," *IEEE Trans. Geosci. Remote Sens.*, vol. 57, no. 11, pp. 8584–8599, Nov. 2019.
[25] D. D'Aria, A. Leanza, A. Monti-Guarnieri, and A. Recchia, "Decorrelating targets: Models and measures," in *Proc. IEEE Int. Geosci. Remote Sens. Symp. (IGARSS)*, Beijing, China, Jul. 2016, pp. 3194–3197.
[26] S. Hobbs *et al.*, "G-CLASS: H_2O, A mission to observe and understand processes of the daily water cycle over land, ESA ref.: CEE10/008," Eur. Space Agency, Paris, France, Tech. Rep. CEE10/008, 2018.
[27] J. T. Koskinen, J. T. Palliainen, J. M. Hyyppa, M. E. Engdahl, and M. T. Hallikainen, "The seasonal behavior of interferometric coherence in boreal forest," *IEEE Trans. Geosci. Remote Sens.*, vol. 39, no. 4, pp. 820–829, Apr. 2001.
[28] S.-K. Lee, F. Kugler, K. P. Papathanassiou, and I. Hajnsek, "Quantification of temporal decorrelation effects at L-band for polarimetric SAR interferometry applications," *IEEE J. Sel. Topics Appl. Earth Observ. Remote Sens.*, vol. 6, no. 3, pp. 1351–1367, Jun. 2013.
[29] L. Eriksson, M. Santoro, A. Wiesmann, and C. Schmullius, "Multitemporal JERS repeat-pass coherence for growing-stock volume estimation of Siberian forest," *IEEE Trans. Geosci. Remote Sens.*, vol. 41, no. 7, pp. 1561–1570, Aug. 2003.
[30] C. Thiel and C. Schmullius, "The potential of ALOS PALSAR backscatter and InSAR coherence for forest growing stock volume estimation in central Siberia," *Remote Sens. Environ.*, vol. 173, pp. 258–273, Feb. 2016.
[31] M. Santoro, U. Wegmüller, and J. Askne, "Forest stem volume estimation using C-band interferometric SAR coherence data of the ERS-1 mission 3-days repeat-interval phase," *Remote Sens. Environ.*, vol. 216, pp. 684–696, Oct. 2018.
[32] J. T. Pulliainen, M. Engdahl, and M. Hallikainen, "Feasibility of multitemporal interferometric SAR data for stand-level estimation of boreal forest stem volume," *Remote Sens. Environ.*, vol. 85, no. 4, pp. 397–409, 2003.
[33] A. Hamadi, L. Villard, P. Borderies, C. Albinet, T. Koleck, and T. L. Toan, "Comparative analysis of temporal decorrelation at P-band and low L-band frequencies using a tower-based scatterometer over a tropical forest," *IEEE Geosci. Remote Sens. Lett.*, vol. 14, no. 11, pp. 1918–1922, Nov. 2017.
[34] L. Villard, T. L. Toan, D. H. T. Minh, S. Mermoz, and A. Bouvet, "Forest biomass from radar remote sensing," in *Land Surface Remote Sensing in Agriculture and Forest*, N. Baghdadi and M. Zribi, Eds. Amsterdam, The Netherlands: Elsevier, 2016, ch. 9, pp. 363–425.
[35] S. El Idrissi Essebtey *et al.*, "Temporal decorrelation of tropical dense forest at C-band: First insights from the TropiScat-2 experiment," *IEEE Geosci. Remote Sens. Lett.*, vol. 17, no. 6, pp. 928–932, Jun. 2020.
[36] S. El Idrissi Essebtey, L. Villard, P. Borderies, T. Koleck, B. Burban, and T. Le Toan, "Comparative study of temporal decorrelation at P, L and C-bands: First insights from the TropiScat-2 experiment," in *Proc. Medit. Middle-East Geosci. Remote Sens. Symp. (MGARSS)*, Tunis, Tunisia, Mar. 2020, pp. 246–249.
[37] H. Aghababaei, G. Ferraioli, and G. Schirinzi, "Polarization analysis of the impact of temporal decorrelation in synthetic aperture radar (SAR) tomography," *Remote Sens.*, vol. 11, no. 6, p. 686, Jan. 2019.
[38] Y. Lei, P. Siqueira, and R. Treuhaft, "A physical scattering model of repeat-pass InSAR correlation for vegetation," *Waves Random Complex Media*, vol. 27, no. 1, pp. 129–152, 2017.
[39] A. R. Monteith and L. M. H. Ulander, "Temporal survey of P-and L-band polarimetric backscatter in boreal forests," *IEEE J. Sel. Topics Appl. Earth Observ. Remote Sens.*, vol. 11, no. 10, pp. 3564–3577, Oct. 2018.
[40] D. H. T. Minh, T. Le Toan, F. Rocca, S. Tebaldini, M. M. d'Alessandro, and L. Villard, "Relating P-band synthetic aperture radar tomography to tropical forest biomass," *IEEE Trans. Geosci. Remote Sens.*, vol. 52, no. 2, pp. 967–979, Feb. 2014.
[41] L. M. H. Ulander, A. R. Monteith, M. J. Soja, and L. E. B. Eriksson, "Multiport vector network analyzer radar for tomographic forest scattering measurements," *IEEE Geosci. Remote Sens. Lett.*, vol. 15, no. 12, pp. 1897–1901, Dec. 2018.
[42] A. R. Monteith and L. M. H. Ulander, "Temporal characteristics of P-band tomographic radar backscatter of a boreal forest," *IEEE J. Sel. Topics Appl. Earth Observ. Remote Sens.*, vol. 14, pp. 1967–1984, Jan. 2021.
[43] J. B. Billingsley, *Low-Angle Radar Land Clutter-Measurements and Empirical Models*. Norwich, U.k.: William Andrew Publishing/Noyes Publishing, 2002.
[44] A. R. Monteith, L. M. H. Ulander, and S. Tebaldini, "Calibration of a ground-based array radar for tomographic imaging of natural media," *Remote Sens.*, vol. 11, no. 24, pp. 1–22, 2019.
[45] J. Cermák, J. Kučera, W. L. Bauerle, N. Phillips, and T. M. Hinckley, "Tree water storage and its diurnal dynamics related to sap flow and changes in stem volume in old-growth Douglas-fir trees," *Tree Physiol.*, vol. 27, no. 2, pp. 181–198, 2007.
[46] S. Pfautsch, T. Hölttä, and M. Mencuccini, "Hydraulic functioning of tree stems—Fusing ray anatomy, radial transfer and capacitance," *Tree Physiol.*, vol. 35, no. 7, pp. 706–722, 2015.
[47] R. Touzi, A. Lopes, J. Bruniquel, and P. W. Vachon, "Coherence estimation for SAR imagery," *IEEE Trans. Geosci. Remote Sens.*, vol. 37, no. 1, pp. 135–149, 1999.
[48] J. Lee and E. Pottier, *Polarimetric Radar Imaging*. Boca Raton, FL, USA: Taylor & Francis, 2009.
[49] A. R. Tice, P. B. Black, and R. L. Berg, "Unfrozen water contents of undisturbed and remolded alaskan silt," *Cold Regions Sci. Technol.*, vol. 17, no. 2, pp. 103–111, Dec. 1989.
[50] J. T. Pulliainen, L. Kurvonen, and M. T. Hallikainen, "Multitemporal behavior of L-and C-band SAR observations of boreal forests," *IEEE Trans. Geosci. Remote Sens.*, vol. 37, no. 2, pp. 927–937, Mar. 1999.
[51] A. Mavrovic *et al.*, "Dielectric characterization of vegetation at L band using an open-ended coaxial probe," *Geosci. Instrum., Methods Data Syst.*, vol. 7, no. 3, pp. 195–208, Jul. 2018.
[52] J. J. Ruiz *et al.*, "SodSAR: A tower-based 1–10 GHz SAR system for snow, soil and vegetation studies," *Sensors*, vol. 20, no. 22, pp. 1–18, Nov. 2020.

Albert R. Monteith (Member, IEEE) received the M.Sc. degree in electrical engineering and the Ph.D. degree in radio and space science from the Chalmers University of Technology, Gothenburg, Sweden, in 2015 and 2020, respectively.

He is a Post-Doctoral Researcher with the Department of Space, Earth and Environment, Chalmers University of Technology. His main research interest lies in the temporal aspects of radar remote sensing of forests.

Lars M. H. Ulander (Fellow, IEEE) received the M.Sc. degree in engineering physics and the Ph.D. degree in electrical and computer engineering from the Chalmers University of Technology, Gothenburg, Sweden, in 1985 and 1991, respectively.

Since 1995, he has been with the Swedish Defence Research Agency (FOI), where he is the Director of Research in Radar Signal Processing and leads the research on very high-/ultrahigh-frequency band radar. Since 2014, he has been a Professor in radar remote sensing with the Chalmers University of Technology. He is the author or coauthor of over 300 professional publications, of which more than 60 are published in peer-reviewed scientific journals. He is the holder of five patents. His research interests include synthetic aperture radar, electromagnetic scattering models, and remote sensing applications.